

Assimilation of magnetic resonance elastography data in an in silico brain model

Felipe Galarce, Karsten Tabelown, Jörg Polzehl, Christos Panagiotis Papanikas,
Vasileios Vavourakis, Ledia Lilaj, Ingolf Sack, Alfonso Caiazzo

April 27, 2022

Abstract

This paper investigates a data assimilation approach for non-invasive quantification of intracranial pressure from partial displacement data, acquired through magnetic resonance elastography. Data assimilation is based on a parametrized-background data weak methodology, in which the state of the physical system – tissue displacements and pressure fields – is reconstructed from partially available data assuming an underlying poroelastic biomechanics model. For this purpose, a physics-informed manifold is built by sampling the space of parameters describing the tissue model close to their physiological ranges, to simulate the corresponding poroelastic problem, and compute a reduced basis. Displacements and pressure reconstruction is sought in a reduced space after solving a minimization problem that encompasses both the structure of the reduced-order model and the available measurements. The proposed pipeline is validated using synthetic data obtained after simulating the poroelastic mechanics on a physiological brain. The numerical experiments demonstrate that the framework can exhibit accurate joint reconstructions of both displacement and pressure fields. The methodology can be formulated for an arbitrary resolution of available displacement data from pertinent images. It can also inherently handle uncertainty on the physical parameters of the mechanical model by enlarging the physics-informed manifold accordingly. Moreover, the framework can be used to characterize, in silico, biomarkers for pathological conditions, by appropriately training the reduced-order model. A first application for the estimation of ventricular pressure as an indicator of abnormal intracranial pressure is shown in this contribution.

1 Introduction

In silico models and computer simulations have enormous potential to provide clinically valuable insights into the mechanics of complex biological tissues. In this context, data assimilation methods are being developed to complement the available data, such as information acquired through medical imaging, *in vitro*, or *in vivo* experiments, with physical models, advanced numerical simulations, and mathematical methods. This paper focuses on the assimilation of internal displacement data, as those acquired in magnetic resonance elastography (MRE) examinations, into a human brain in silico model.

MRE is a medical imaging modality designed to measure mechanical properties of biological tissues. It combines phase-contrast MRI with the propagation of harmonic mechanical waves (10–100 Hz) induced by actuators placed externally on the patient body surface [1]. The mechanical response of the tissue is recorded as a three-dimensional *internal* displacement field. Combined with physical tissue models and different inversion methods, these displacement data allow to obtain quantitative information on tissue mechanical properties, e.g., in terms of mechanical parameters (see [2, 3, 4]).

The clinical potential of elastography has been constantly increasing in the last decades [5]. It has been proven to be an effective approach for the quantitative estimation of biomarkers (such as elastic parameters, tissue fluidity, viscoelasticity) related to tissue pathologies. Relevant clinical applications of MRE include diagnosis and staging of pathologies that have a direct influence on tissue stiffness, such as cancer and fibrosis [6, 7, 8]. Focusing on the brain, elastography has been used for the characterization of cancer tissue [9] and for the early stage diagnosis of neurological diseases characterized by alteration of microstructure properties of brain tissue (see [10]).

This work is motivated by the applicability of elastography in monitoring and quantifying the increase of intracranial pressure (ICP), i.e., the increase of cerebro-spinal fluid (CSF) in the ventricles within the brain, which yields a pressure increase on the brain. Intracranial hypertension might be responsible of different neurological diseases, such as ischemia, tumors, and hydrocephalus [11]. Moreover, this pathological conditions might be responsible of neurological disturbances and cerebral damages. Recent research focused on the correlation between hydrocephalus and changes in the elastic behavior (see [12] or the recent review [13]). In [14] a novel method based on ultrasound time-harmonic elastography has been described, in which the quantification of shear wave speed is used as indirect biomarker for elevated ICP. This paper presents a data assimilation pipeline to infer the interplay between an increase in ICP and the mechanical response of brain tissue to harmonic waves. Hence, the goal of this paper is to propose, for the first time, a computational method for non-invasive quantification of elevated ICP from internal displacement data. Currently, precise measurement of ventricular pressure and ICP is based on invasive procedures such as catheterization or perforation and, hence, not suited for early stage risk quantification and constant monitoring. Non-invasive alternatives for the estimation of relevant pressure gradients would consequently drastically enhance the possibilities for early-stage diagnosis and patient monitoring. In order to characterize the fluid pressure field within the brain tissue, it is necessary to consider a biphasic tissue model describing both the solid and the fluid (i.e., the ICP) mechanics.

Recent experimental results suggested that, accounting for the fluid phase, MRE can be utilized to infer the presence of pathological pressure conditions, by measuring the effect of the increase in interstitial pressure on tissue mechanics [15, 16, 17]. More recent studies address different applications of MRE with a biphasic model of the tissue, e.g., a poroelastic medium, in which the solid and interstitial fluid interactions have been investigated [18, 19, 20, 21, 18, 22].

Computational modeling of brain biomechanics is a challenging problem, due to the structural complexity of the brain, and to the lack of suitable experimental data for model parametrization. Biomechanical models of the human brain based on in vitro mechanical experiments have been recently studied in [23], while a detailed discussion of suitable constitutive models for brain tissue based on in silico experiments has been presented in [24]. Focusing on hydrocephalus, the mechanics of ventricle growth has been computationally investigated in [25] using a realistic three-dimensional single-phase brain model based on hyperelastic constitutive law. Biphasic (poro-viscoelastic) models have been investigated in [26], performing load experiments in silico to computationally investigate the response of the tissue. The choice of the brain mechanical model shall be dictated by the regime of dynamics of interest and by the targeted application [27]. While hyperelastic laws are suited for capturing long-term dynamics, this paper focuses on a linear poroelastic description, which is assumed to be able to describe fast phenomena such as the vibration induced by MRE, e.g., [28].

Despite the linearity of the model, this problem is extremely demanding for two major reasons: (i) the high dimension of the unknowns (the pressure field, defined at each point of a suitable discretization of the brain) and, (ii) the limited availability and resolution of data. In fact, MRE acquisition is practically constrained by the length of examination time, and displacement data are typically available only on a sub-region of the tissue of interest. In addition, non invasive experimental measurement are normally only available for the displacement field.

A finite element method for reconstructing poroelastic parameters from MRE was first presented in [29, 30], by considering a synthetic phantom. A numerical framework for the estimation of poroelastic tissue pressure from MRE data has been recently proposed in [31]. The method is based on solving Biot problems locally in different patches located in the region where MRE data are available. To overcome the lack of pressure boundary conditions in the measurement regions, the displacement data are used to derive suitable expressions for the pressure on the boundary. The results of Tan *et al.* [31] are limited to a numerical phantom (cubic tissue sample with a single inclusion). However, their approach still faces several challenges related to robustness (noisy data) and due to the high number of unknown parameters, including the internal pressure boundary conditions between the patches. A different approach for the estimation of the pressure field in the context of MRE has been recently proposed by Fovargue and colleagues [32, 33], combining a stiffness reconstruction approach (also for large strains) with an analytic model of an inflating sphere to relate it to the pressure field.

The overarching goal of this paper is to assimilate MRE data of poroelastic biological tissues into in silico modeling from the perspective that in clinical applications only partial measurements – few slices, and with limited resolution – are available. Thus, focusing here on brain elastography, ‘reconstruction’ of a poroelastic solution (both displacement and pressure fields) over the whole computational domain, the brain organ, is put in challenge. Full organ *reconstruction* is vital to infer pressure-dependent biomarkers, if the regions of interests are not fully contained in the imaged subdomain. This is the case, for instance, of the ventricular CSF pressure, which can be considered as an indicator of hydrocephalus. The considered reconstruction algorithm addresses the state estimation problem based on the parametrized-background data-weak (PBDW) method [34]. Originally introduced for wave equations, the PBDW has been recently extended in the context of ultrasound and PC-MRI images of blood flow [35, 36, 37]. This approach is designed to reconstruct a physical solution over the whole domain given only partial displacements information. The reconstruction algorithm is based on full anatomical information, in order to create a finite element model, and a background parametrized PDE. The underlying physics is then exploited to extend the available measurement to a function defined in the whole three-dimensional brain model (Figure 1).

To solve the problem one generates a manifold of suitable solutions, a training set, of the underlying PDE sampling the parameter space. Hence, the method avoids the issue of setting internal pressure boundaries and can naturally take into account a small variability in the physical and mechanical parameters. Then, the state reconstruction is sought on a low-dimensional subspace of this PDE-informed manifold, solving an optimization problem depending on which the available observations are included via linear constraints. The method can be interpreted as a predictor-corrector scheme, in which a solution belonging to the low-dimensional subspace of the training set is improved by adding a correction, orthogonal to the subspace, that accounts for the model bias [35, 34].

The main contribution of this work is twofold: First, a detailed validation of PBDW in the context of brain elastography is presented. The validation is based on a pipeline with multidisciplinary components, entailing multi-modal image acquisition, data processing and image segmentation, in silico model generation, numerical solution, and data assimilation. In this paper, the assimilated displacement data are limited to synthetic measurements. However, the computational setup considers a physiological brain model, and the synthetic data have been defined in such a way to mimic a realistic experimental setup used in recent clinical research works [19]. Second, the framework is used for the characterization of pressure-dependent biomarkers such as the ventricular pressure, to characterize pathological ICP gradients. In particular, this characterization is done using only elastography data on a subset of the domain, not necessarily including the ventricles. For the present application demonstration, two populations of synthetic patients are created, classified into a healthy and an unhealthy group. The pathological states are characterized by a pressure increase in the ventricle by 10% with respect to the healthy ones. For

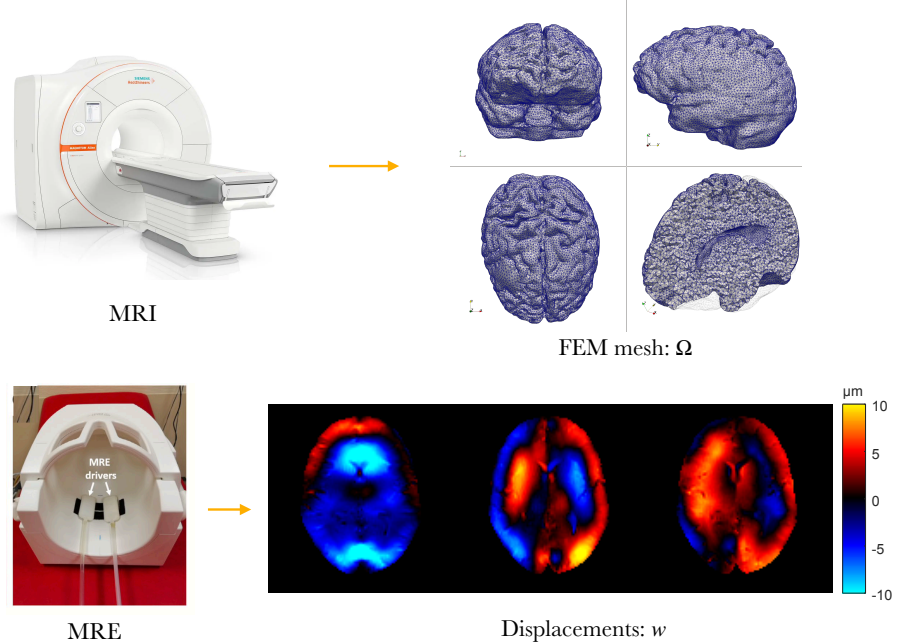


Figure 1: The purpose of the considered data assimilation algorithm is to map partially available MRE measurements acquired on few slices onto a displacement field defined on a three-dimensional brain model. As an example, a typical wave image on a slice is shown in the bottom sketch. The mapping requires anatomical data to construct the brain model and it is based on assuming an underlying tissue model (encoded in a PDE), which is numerically solved via a finite elements to construct a suitable space for the reconstruction (top sketch).

both cases, forward numerical simulations are performed, sampling displacement data on few slices at the level of the eyes. By properly constructing the training set for the reconstruction, the data assimilation algorithm is able to correctly classify all cases in the corresponding group. The application of the proposed framework to *in vivo* displacement data is currently under investigation, combined with novel pre-processing techniques to estimate tissue properties from MRI data [19, 38].

The rest of the paper is organized as follows. Section 2 introduces the PBDW data assimilation framework from a general perspective, while Section 3 describes the considered poroelastic model and the numerical method used for the solution. The application of the PBDW to the particular context is detailed in Section 4. The validation in the case of synthetic MRE measurements and the application to hydrocephalus classification are shown in Section 5, while the conclusions are drawn in Section 6.

2 A framework for data assimilation

The proposed numerical framework is based on the Parametrized Background Data-Weak (PBDW) method for state estimation, originally proposed in [39], and recently applied also in the context of hemodynamics problems [35, 40].

Let us consider a physical domain $\Omega \subset \mathbb{R}^d$ ($d = 2, 3$), and let us assume that tissue biomechanics is described by a parameter-dependent partial differential equation \mathcal{P} of the form

$$\mathcal{P}(u, \theta) = 0, \quad (2.1)$$

which will be referred thereafter as the *forward model*. In (2.1), $u \in V$ denotes the *state*, and $\theta \in \mathbb{R}^P$ stands for an array of *parameters*.

The rest of this section is dedicated to the description of the pipeline for the data assimilation of a general forward model and general observations, introducing the main notations and the different computational steps. In Section 3, it will be shown how to apply the framework to the particular case of a forward model based on the Biot equations – the state u consists of displacement and pressure fields – and to the case of observations defined by MRE data.

2.1 PBDW preliminaries

The space V (also called the *ambient space*) is a functional space suitable for well-posing the forward problem (2.1). It will be assumed to be a Hilbert space, endowed with an inner product (denoted by $\langle \cdot, \cdot \rangle$) and with the induced norm $\|\cdot\| = \sqrt{\langle \cdot, \cdot \rangle}$. Depending on the PDE under consideration, typical choices for V are subspaces of $L^2(\Omega)$ or $H^1(\Omega)$ (or product spaces of those), with the corresponding standard inner products.

Moreover, let us consider an appropriate discretization of the forward model (2.1) using the finite element method. As such, let us introduce a computational mesh \mathcal{T}_h of the domain Ω of characteristic size h , and let us denote with V_h a finite element space defined on \mathcal{T}_h . The dimension of the discrete space V_h is denoted by \mathcal{N} , i.e., the number of degrees of freedom per discrete (nodal) point of the finite element mesh. Moreover, it is also assumed that V_h satisfies suitable approximation properties with respect to the ambient space V .

In what follows, (\cdot, \cdot) will denote the inner product for the particular case of $L^2(\Omega)$. Moreover, Π_U will denote the orthogonal projector on a subspace $U \subset V_h$. Finally, \mathcal{L}_i , $i = 1, \dots, \mathcal{N}$ will denote the basis functions of the finite element space, while $M \in \mathbb{R}^{\mathcal{N} \times \mathcal{N}}$ will stand for the mass matrix that defines the Hilbertian setting of the considered finite element space and the corresponding norm, i.e., for the L^2 -setting:

$$M_{ij} := \int \mathcal{L}_i, \mathcal{L}_j \, dx. \quad (2.2)$$

2.2 The space of observations

The first step to formalize the data assimilation problem consists in the construction of a functional space of observations. To this purpose, let l_1, \dots, l_m be a set of m independent observations, assumed to be modeled by m independent linear functionals $\ell_i : V_h \rightarrow \mathbb{R}$ ($i = 1, \dots, m$) applied to an underlying *true* solution $u_{\text{true}} \in V_h$, i.e., $l_i = \ell_i(u_{\text{true}})$. This might be the case, for instance, of image data (or, in general, any sensor data).

These assumptions allows to define a finite dimensional space of observations $W = \text{Span}(w_1, \dots, w_m)$, with $W \subset V_h$, spanned by the unique Riesz representer of the observation functionals ℓ_i , i.e., so that it holds

$$\ell_i(u_{\text{true}}) = \langle u_{\text{true}}, w_i \rangle, \text{ for } i = 1, \dots, m.$$

Without loss of generality, we assume that $\|w_i\| = 1$ for $i = 1, \dots, m$, and that $\langle w_i, w_j \rangle = 0$ for any $i \neq j$ (orthonormality can otherwise be imposed in a post-processing step). Thus, the input data (i.e., the set of available measurement) is modeled via a function $w \in W$ that is defined by the projection of the true solution onto W : $w = \sum_i \ell_i(u_{\text{true}}) w_i = \Pi_W u_{\text{true}}$. The data assimilation problem under

investigation can be formalized as finding a measure-to-state operator $\mathcal{A} : W \rightarrow V_h$, which, given a set of observation $w \in W$, finds a suitable state $u^* \in V_h$ that approximates u_{true} , in the sense $\|u^* - u_{\text{true}}\|$ is small.

2.3 Data assimilation as a minimization problem

The problem of estimating $u^* \in V_h$ solely relying on the data $w \in W$ is ill-posed. To overcome this issue, information about the dynamics of the state u_{true} encoded in the forward problem (2.1) shall be incorporated. Namely, a manifold of solutions (the ‘parametrized background’) of the underlying dynamics (2.1) is introduced

$$\mathcal{M} = \{u \in V_h; \mathcal{P}(u, \theta) = 0, \theta \in \Theta\}, \quad (2.3)$$

encompassing a range of governing dynamics as broad as the dimension of the parameter space $\Theta \subset \mathbb{R}^p$. The dimension of the manifold \mathcal{M} depends on the size of the discretization \mathcal{N} employed to solve numerically the underlying dynamics.

Remark 2.1 (Parameter space). *The parameter space Θ used to define the manifold (2.3) can be chosen a subset of the suitable parameter space for the forward model (see Section 2.4). Therefore, one can incorporate in the data assimilation framework any additional knowledge on the problem parameters such as, e.g., initial estimates or variability relevant for the problem of interest.*

Under the assumption that the resulting dynamics has a fast decaying Kolmogorov n -width and, therefore, that the dynamics can be well approximated with a suitable reduced-order model, we introduce a reduced-order space $V_n \subset \mathcal{M}$ with dimension $n \ll \dim \mathcal{M}$, such that $\max_{u \in \mathcal{M}} \|\Pi_{V_n} u - u\| < \epsilon(V_n)$ for some (small) $\epsilon(V_n) > 0$.

The methodology is formalized by the following constrained minimization problem [39]:

Problem 2.2 (PBDW). *Find $u^* \in V$, $v^* \in V_n$ and $\eta^* \in V$ such that $\inf_{u,v} \|\eta(u, v)\|$ and*

$$\begin{aligned} \langle \eta, z \rangle &= \langle u, z \rangle - \langle v, z \rangle \quad \forall z \in V \\ \langle u, q \rangle &= \langle u_{\text{true}}, q \rangle \quad \forall q \in W \end{aligned} \quad (2.4)$$

Detailed analysis of problem 2.2, including its convergence properties for increasing m (i.e., the number of available observations), can be found in [39]. However, an overview of the relevant aspects for the application to the case of MRE data is briefly given below.

Remark 2.3. *Notice the test space in (2.4)₂ introduces the constraint on the available measurements through the coefficients in the basis (w_1, \dots, w_m) of W . Namely, taking $q = w_i$, from (2.4)₂ it follows that $\ell_i(u^*) = \langle w_i, u_{\text{true}} \rangle = \ell_i(u_{\text{true}})$.*

In addition, for the variational approximation via (2.4) the following *a priori* error estimation holds (see [41]):

$$\|u^* - u_{\text{true}}\| \leq \beta(V_n, W)^{-1} \epsilon_n(V_n), \quad (2.5)$$

where

$$\beta(V_n, W) = \inf_{v \in V_n} \frac{\|\Pi_W v\|}{\|v\|}, \quad (2.6)$$

is an inf–sup stability constant that can be interpreted geometrically as the angle between spaces V_n (reduced space of solutions) and W (observations).

Otherwise stated, $\beta(V_n, W)$ measures the *observability* of the reduced space V_n based on the type of available measurements. Namely, for a fixed number of observations, m , the richer the reduced space

is (i.e., the larger its dimension n), the more likely will be to find elements that are hardly observable with the given set of measurement – or, equivalently, which lie orthogonal to W – hence deteriorating the algorithm stability according to (2.5).

Estimate (2.6) introduces therefore a trade-off between the approximation quality of the reduced-order model, $\epsilon(V_n)$, and the observability, $\beta(V_n, W)$. This relation is typically used to choose the dimension of the space V_n . For instance, in [41], a so-called *nested space* strategy is followed to select the dimension of the reduced-order model such that the *a priori* bound (2.6) is minimized.

It can be shown [39] that, for the optimal state, it holds $u^* \in V_n \oplus (W \cap V_n^\perp)$. In addition, Problem 2.2 can be reformulated as: Find

$$u^* = \arg \min_{u \in V_h} \|\Pi_{V_n^\perp} u\|^2, \text{ such that } \langle w_i, u \rangle = \ell_i(u), i = 1, \dots, m. \quad (2.7)$$

In Section 2.5 we will derive the algebraic formulation of the optimal condition for (2.7), and discuss in detail the practical construction of the linear space V_n from discrete samples of the background governing dynamics.

Definition 1 (Measure-to-state operator). In view of (2.7), we define the operator $\mathcal{A} : W \rightarrow V_h$ by

$$\mathcal{A}(w) := \arg \min_{V_h} \|\Pi_{V_n^\perp} u\|^2, \text{ such that } \langle w_i, u \rangle = \langle w_i, l \rangle = l_i, i = 1, \dots, m. \quad (2.8)$$

2.4 Training phase

Let us consider K samples from the parameter set, denoted as $y_1, \dots, y_K \in Y$. Also, and let us introduce a set $\mathcal{M}^{\text{training}} \subset \mathcal{M}$ containing ‘snapshots’ of the governing dynamics, defined by $\mathcal{M}^{\text{training}} = \{u^1, \dots, u^K, \text{ such that } \mathcal{P}(u^i, y_i) = 0, i = 1, \dots, K\}$, i.e., by the snapshots $u^1, \dots, u^K, u^i \in V_h$, which are finite element solutions for the considered parameter samples.

The high-dimensional dataset above will be compressed into a reduced-order model of a smaller dimension that can still approximate the governing dynamics. The reduced space $V_n^h \subset V_n$ is constructed by means of a principal component analysis (PCA; also called proper orthogonal decomposition, see [42]). The basis of this space is computed by introducing the covariance matrix $C \in \mathbb{R}^{K \times K}$ whose entries are given by $C_{ij} = \langle u^i, u^j \rangle$, and computing an eigenvalue decomposition $C = V \Lambda V^T$ for $\Lambda \in \mathbb{R}^{K \times K}$ and $V \in \mathbb{R}^{K \times K}$. The reduced basis that spans V_n can be then obtained from the first n columns, ordered according to the eigenvalues (from highest to lowest), of the matrix $U = S^{-1}AV$, where $S_i^2 = \Lambda_i$, for $i = 1, \dots, \min\{K, \mathcal{N}\}$, and A is the so-called *snapshots matrix*, whose columns corresponds to the snapshots $u^i, i = 1, \dots, K$.

Remark 2.4. *The approach described above to compute the reduced basis is computationally favorable if $K \ll \mathcal{N}$ – this is the case for numerical experiments presented in the following sections. When $K \gg \mathcal{N}$ the PCA is typically performed with the covariance matrix $C = \sum_{i=1}^K u_i \otimes u_i$, which has dimension $\mathcal{N} \times \mathcal{N}$.*

Assuming that the eigenvalues are numbered according to decreasing order $\Lambda_1 \geq \Lambda_2 \geq \dots \geq \Lambda_{\max\{K, \mathcal{N}\}} > 0$, a normalized version of the model error in the *a priori* bound (2.6) is given by

$$\hat{\epsilon}_n = \left(\sum_{i=1}^{\max\{\mathcal{N}, K\}} \Lambda_i \right)^{-1/2} \left(\sum_{i=n+1}^{\max\{\mathcal{N}, K\}} \Lambda_i \right)^{1/2}. \quad (2.9)$$

In principle, (2.9) serves to assert the quality of the reduced model.

2.5 Optimality conditions of the PBDW

Let $\Phi = (\rho_1 | \dots | \rho_n) \in \mathbb{R}^{\mathcal{N} \times n}$ be the matrix whose columns contains the reduced basis. The matrix representation of the operator $\Pi_{V_n^h} : V_h \rightarrow V_n$ can be characterized as

$$\Pi_{V_n^h} u = \Phi \Phi^T M u, \quad \forall u \in V_h. \quad (2.10)$$

Similarly, introducing the matrix $\mathcal{W} \in \mathbb{R}^{\mathcal{N} \times m}$ whose columns are the Riesz representers of the measurements, w_1, \dots, w_m , the projection onto W^h can be expressed via

$$\Pi_{W^h} u = \mathcal{W} \mathcal{W}^T M u, \quad \forall u \in V_h. \quad (2.11)$$

Let $l := (\ell_i(u_{\text{true}}))_i$ be the vector of available measurements. Using (2.10) and (2.11), the Lagrangian for the minimization problem (2.7) can be now written as follows:

$$\begin{aligned} \mathcal{L}(u; \lambda) &= \|u - \Pi_{V_n^h} u\|^2 - \lambda^T (\mathcal{W}^T M u - l) \\ &= \left((I - \Phi \Phi^T M) u \right)^T M \left((I - \Phi \Phi^T M) u \right) - \lambda^T (\mathcal{W}^T M u - l) \\ &= u^T M (I - \Phi \Phi^T M) u - \lambda^T (\mathcal{W}^T M u - l). \end{aligned} \quad (2.12)$$

The last equality holds since the projector operator onto V_n^\perp , i.e., $(I - \Phi \Phi^T M)$, is both symmetric and idempotent.

The following results show that the minimization problem defining the operator \mathcal{A} (2.8) can be formulated using the language of filtering approaches.

Proposition 2.5. *Problem (2.7) admits a solution of the form $u^* = v^* + \eta^*$, with*

$$v^* = \Phi \left[\left(G^T G \right)^{-1} G^T l \right], \quad (2.13)$$

where the cross-Gramian $G \in \mathbb{R}^{m \times n}$ is defined by $G_{ij} = \langle w_i, \rho_j \rangle$, or $G = \mathcal{W}^T M \Phi$, and

$$\eta^* = \mathcal{W} \mathcal{W}^T M v^* - w, \quad (2.14)$$

with $w = \mathcal{W} l$.

Proof. The Euler-Lagrange (EL) equations for (2.12) reads

$$\begin{pmatrix} I - \Phi \Phi^T M & -\mathcal{W} \\ \mathcal{W}^T & 0 \end{pmatrix} \begin{pmatrix} u \\ \lambda \end{pmatrix} = \begin{pmatrix} 0 \\ l \end{pmatrix}, \quad (2.15)$$

with $\lambda \in \mathbb{R}^m$. An alternative could be to solve directly for (u, λ) this saddle point problem. Nonetheless, is much more convenient to consider the orthogonal decomposition $u = v + \eta$, with $v \in V_n^h$ and $\eta \in V_n^{h, \perp} = \text{Ker}(\Pi_{V_n^h})$. Since $\Pi_{V_n^{h, \perp}} u = \eta$, from (2.15) we obtain

$$(I - \Phi \Phi^T M) u - M \mathcal{W} \lambda = \eta - \mathcal{W} \lambda = 0 \Rightarrow \mathcal{W}^T \eta = \lambda. \quad (2.16)$$

Multiplying by $\Phi^T M$ leads to:

$$\Phi^T M (\eta - \mathcal{W} \lambda) = \underbrace{\Phi^T M \mathcal{W}}_{G^T} \lambda = 0. \quad (2.17)$$

where we have introduced the definition $G = \mathcal{W}^T M \Phi$.

Let now $c = (c_1, \dots, c_n) \in \mathbb{R}^n$ be the coordinates of v in the basis Φ , i.e. $v = \Phi c$. From (2.15) we obtain

$$\mathcal{W}^T M \Phi c + \mathcal{W}^T \eta = l. \quad (2.18)$$

Multiplication by G^T yields

$$G^T l = G^T G c + G^T \mathcal{W}^T \eta \underset{(2.16)}{=} G^T G c + G^T \lambda \underset{(2.17)}{=} G^T G c. \quad (2.19)$$

Solving for c in (2.19) and using $v = \Phi c$ yields (2.13), while Equation (2.14) follows from (2.18). \square

The operator $\mathcal{A}(w)$ sought can be thus decomposed in a prediction, $v^* \in V_n$, and a correction, $\eta^* \in V_n^\perp \oplus W$, component respectively. The former belongs to the considered reduced-order model of the parametric dynamics, while the latter depends on the discrepancy between the prediction and the data.

3 Modeling human brain biomechanics

This paper targets the application of the data assimilation framework described in Section 2 to the case of brain elastography. To this purpose, we model the brain tissue as a poroelastic media, composed of a biphasic mixture of solid gray matter, solid white matters and cerebro-spinal fluid. The brain biomechanics is assumed to obey Biot's equations of poroelasticity [29], the theory of which describes the behavior of the tissue at the mesoscale considering the interaction between biphasic material strains and increments in fluid volume.

3.1 Brain poroelastic model

Derivation of the poroelasticity equations is briefly outlined in this paragraph. Let $\Omega \subset \mathbb{R}^3$ denote the computational domain, whose boundary $\partial\Omega$ is decomposed into disjoint sets: $\partial\Omega = \Gamma_{\text{neck}} \cup \Gamma_{\text{ventricles}} \cup \Gamma_{\text{MRE}}$. Γ_{neck} denotes the portion of the boundary where the displacement vector field is zero, Γ_{MRE} is the boundary where a harmonic pulse (to replicate an MRE pulse) is prescribed, and $\Gamma_{\text{ventricles}}$ stands for the internal boundary between brain tissue and ventricles (see Figure 2).

Let T denote the length of the considered time interval. Soft tissue biomechanics is described by the solid displacements $\mathbf{u} : \Omega \times [0, T] \rightarrow \mathbb{R}^3$, the interstitial fluid pressure $p : \Omega \times [0, T] \rightarrow \mathbb{R}$, and the filtration velocity $\mathbf{z} : \Omega \times [0, T] \rightarrow \mathbb{R}^3$ fields. The governing equations of poroelasticity are derived from conservation laws for mass and momentum, taking into account the interplay between (solid and fluid) material strains and local increments in fluid volume. The balance equations of linear momentum read

$$\rho \partial_{tt} \mathbf{u} - \nabla \cdot \boldsymbol{\sigma}(\mathbf{u}) + \alpha \nabla p = \mathbf{0} \quad \text{in } \Omega \times [0, T]. \quad (3.1)$$

In (3.1), ρ stands for the solid mass density, and the stress (second-order symmetric) tensor $\boldsymbol{\sigma}(\mathbf{u})$ is related to the corresponding strain tensor by Hooke's law

$$\boldsymbol{\sigma}(\mathbf{u}) = \frac{E}{1+\nu} \boldsymbol{\varepsilon} + \frac{E\nu}{(1+\nu)(1-2\nu)} \text{tr}(\boldsymbol{\varepsilon}) \mathbb{I},$$

where E and ν are Young's modulus and Poisson ratio of the tissue respectively. Moreover, \mathbb{I} is the identity matrix in \mathbb{R}^d , and $\boldsymbol{\varepsilon}$ denotes the symmetric strain deformation tensor, i.e., $\boldsymbol{\varepsilon}(\mathbf{u}) = \frac{1}{2} (\nabla \mathbf{u} + (\nabla \mathbf{u})^T)$. Parameter α in (3.1) is the Biot-Willis parameter which quantifies the coupling between the stress due to the increment of interstitial pressure and the wave propagation stress in the solid matrix. In Equation (3.1) we neglected the contribution of the fluid inertia, assuming that during MRE the relative displacement of the fluid is negligible.

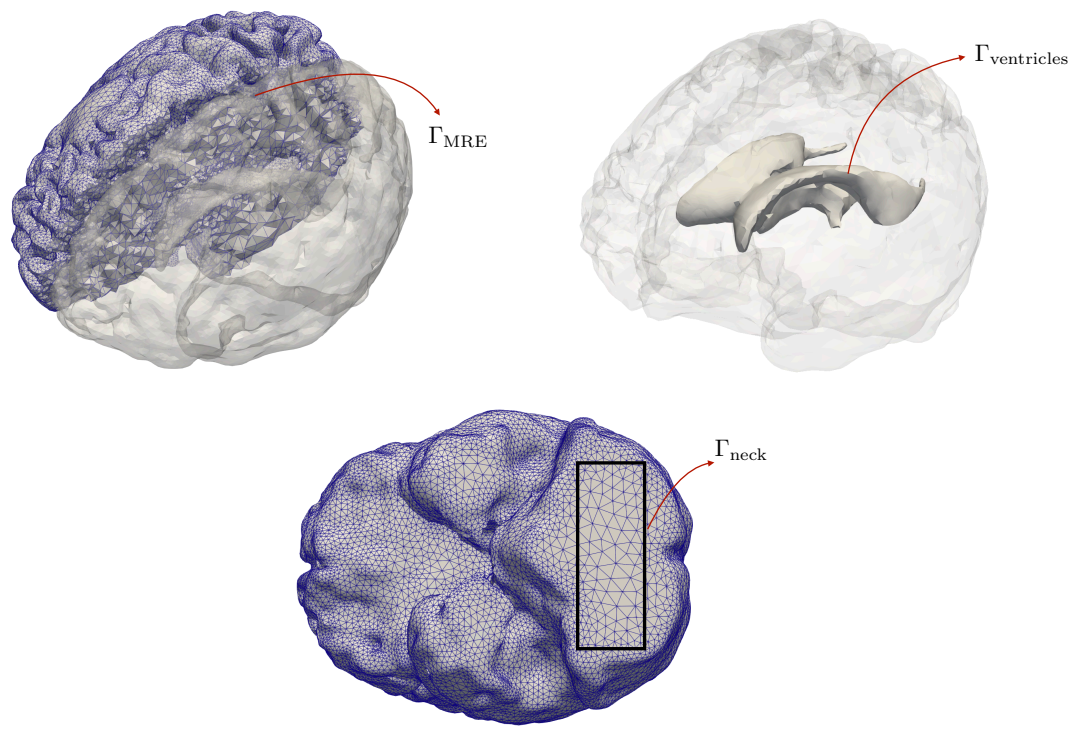


Figure 2: Working domain Ω and the boundary decomposition.

Biofluid flow dynamics in the porous medium is modeled using Darcy's law

$$\mathbf{z} + \frac{\kappa}{\mu} \nabla p = \mathbf{0} \quad \text{in } \Omega \times [0, T], \quad (3.2)$$

where κ is the mixture permeability and μ is the fluid viscosity. The system of PDEs (3.1)–(3.2) is closed by a mass balance equation that accounts for the increment in fluid content and for fluid- and solid-phase velocities:

$$S_\epsilon \partial_t p + \nabla \cdot \partial_t \mathbf{u} + \nabla \cdot \mathbf{z} = 0 \quad \text{in } \Omega \times [0, T]. \quad (3.3)$$

The mass storage parameter is described through: $S_\epsilon = 3\alpha(1 - \alpha B)(1 - 2\nu)(BE)^{-1}$, as a function of the Biot-Willis parameter, the elastic parameters, E and ν , and Skempton's parameter, B . For brain tissue described as a saturated medium, we choose to set $\alpha = 1$. and $B = 0.99$ [43].

Taking the divergence of (3.2) and inserting the result into (3.3) leads to the elimination of the fluid velocity \mathbf{z} . Together with (3.1), one obtains the following system of PDEs for the displacement and the pressure fields:

$$\begin{aligned} \rho \partial_{tt} \mathbf{u} - \nabla \cdot \boldsymbol{\sigma}(\mathbf{u}) + \alpha \nabla p &= 0 \quad \text{in } \Omega \times [0, T] \\ S_\epsilon \partial_t p + \alpha \nabla \cdot \partial_t \mathbf{u} - \frac{\kappa}{\mu} \nabla^2 p &= 0 \quad \text{in } \Omega \times [0, T]. \end{aligned} \quad (3.4)$$

The system is closed by homogeneous initial conditions and by the following boundary conditions

$$\begin{aligned} \boldsymbol{\sigma} \cdot \mathbf{n} &= \mathbf{g}_{\text{MRE}} & \text{on } \Gamma_{\text{MRE}} \\ p &= p_{\text{ventricles}} & \text{on } \Gamma_{\text{ventricles}} \\ \mathbf{u} &= \mathbf{0} & \text{on } \Gamma_{\text{neck}} \\ p &= p_{\text{csf}} & \text{on } \Gamma_{\text{MRE}} \end{aligned}, \quad (3.5)$$

with p_{csf} and $p_{\text{ventricles}}$ denoting the CSF pressure imposed on the outer CSF and on the ventricles, respectively, while the load \mathbf{g}_{MRE} imposed for a Neumann boundary condition on Γ_{MRE} has been defined with the purpose of mimicking the forces on the brain tissue in a MRE examination. Thus, the forcing term has been modeled via: $\mathbf{g}_{\text{MRE}}(\mathbf{x}, t) = \xi \sin(2\pi\omega t) \mathbf{s}(\mathbf{x})$, i.e., a mono-harmonic pulse (with a given cyclic frequency ω and amplitude ξ) multiplied by a space-depending function $\mathbf{s}(\mathbf{x})$ equal to unity where the pulse is applied (back of the brain) and linearly decreasing towards the front of the brain (see Figure 3), i.e.: $\mathbf{s}(\mathbf{x}, y, z) = (1 - y/L)$, where $L = 16.86$ cm is the geometry length along the y-axis (frontal axis). This model is motivated by the need of accounting for the effect of the rigid skull on the propagation of the mechanical force over the whole brain surface.

The model parameters applicable for all simulations setup are summarized in Table 1.

3.2 FE discretization and numerical solution

The system of equations (3.4) is numerically solved using the finite element method (FEM). To this purpose, let \mathcal{T}_h denote a tetrahedral unstructured mesh that discretizes the computational domain Ω – the characteristic size of the mesh is expressed through h . We introduce the functional spaces

$$\begin{aligned} U &= H^1(\Omega)_0^d := \{ \mathbf{v} \in H^1(\Omega) \mid \mathbf{v} = 0 \text{ on } \Gamma_{\text{neck}} \} \\ P &:= H^1(\Omega), \quad Q := \{ q \in H^1(\Omega) \mid q = 0 \text{ on } \Gamma_{\text{ventricles}} \cup \Gamma_{\text{MRE}} \dots \} \end{aligned}$$

and their discrete approximation by linear FE spaces

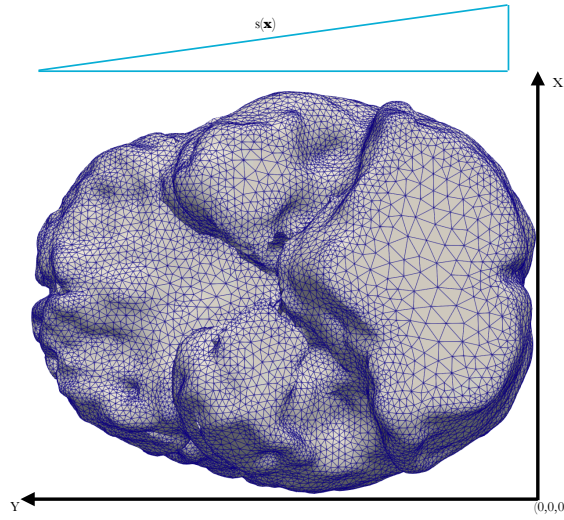


Figure 3: Sketch of the model used for boundary conditions. To mimic the MRE setting, a harmonic force with given amplitude and frequency has been multiplied by a linearly decreasing function $s(x)$ whose values (blue sketch on top) range from one – where the mechanical pulse is applied – to zero, along the direction of the pulse force.

Parameter	Description	Value [Unit]	Reference
α	Biot-Willis parameter	1.0	[43]
μ	Fluid viscosity	10^{-2} P	[43]
ρ	Solid matrix density	1.0 gr/cm ³	[43]
κ	Tissue permeability	$[10^{-9}, 10^{-8}] \text{ cm}^2$	[43]
E	Solid matrix Young Modulus	$[10^5, 10^6] \text{ dyn/cm}^2$	[43]
ν	Solid matrix Poisson's ratio	[0.40, 0.45]	[43]
w_{MRE}	MRE frequency	50 Hz	[44]
p_{csf}	CSF pressure	10^4 dyn/cm^2	[45]
$p_{\text{ventricles}}$	Ventricular pressure	$[1.0, 1.1] \times 10^4 \text{ dyn/cm}^2$	[45]
B	Skempton parameter	0.99	[43]
ξ	Pulse magnitude	-500 dyn	*

Table 1: Parameters used in the poroelastic model and manifold generation.

(*) The value of the pulse excitation magnitude, ξ , has been tuned so that brain tissue deformation simulation outputs are physiologically realistic.

$$\begin{aligned}
U_h &:= \{\mathbf{v} \in U \mid \mathbf{v}|_T \in \mathbb{P}_1(T), \forall T \in \mathcal{T}_h\} , \\
P_h &:= \{q \in P \mid q|_T \in \mathbb{P}_1(T), \forall T \in \mathcal{T}_h\} , \\
Q_h &:= \{q \in Q \mid q|_T \in \mathbb{P}_1(T), \forall T \in \mathcal{T}_h\} .
\end{aligned}$$

Then, we consider the following discrete weak formulation of (3.4): Find $(\mathbf{u}_h, p_h) \in V_h := U_h \times P_h$ such that:

$$\begin{aligned}
\rho(\partial_{tt}\mathbf{u}_h, \mathbf{v}_h) + 2E(\boldsymbol{\varepsilon}(\mathbf{u}_h), \boldsymbol{\varepsilon}(\mathbf{v}_h)) + \lambda(\boldsymbol{\nabla} \cdot \mathbf{u}_h, \boldsymbol{\nabla} \cdot \mathbf{v}_h) + \alpha(\boldsymbol{\nabla} p_h, \mathbf{v}_h) &= (\mathbf{g}_{\text{MRE}}, \mathbf{v})_{\Gamma_{\text{MRE}}} \\
(S_\epsilon \partial_t p_h, q_h) + (\alpha \boldsymbol{\nabla} \cdot \partial_t \mathbf{u}_h, q_h) + \left(\frac{\kappa}{\mu} \boldsymbol{\nabla} p_h, \boldsymbol{\nabla} q_h \right) &= 0,
\end{aligned}$$

for all $(\mathbf{v}_h, p_h) \in U_h \times Q_h$. Discretizing the time derivatives with an implicit Euler scheme and denoting with τ the time step, the time-discrete formulation can be written as

$$A((\mathbf{u}^{n+1}, p^{n+1}), (\mathbf{v}, q)) = \rho \left(\frac{2\mathbf{u}_h^n - \mathbf{u}_h^{n-1}}{\tau^2}, \mathbf{v}_h \right) + (S_\epsilon p_h^n, q_h) + (\alpha \boldsymbol{\nabla} \cdot \mathbf{u}_h^n, q_h) , \quad (3.6)$$

where the form

$$\begin{aligned}
A((\mathbf{u}, p), (\mathbf{v}, q)) &:= \left(\frac{\rho}{\tau^2} \mathbf{u}_h, \mathbf{v}_h \right) + 2E(\boldsymbol{\varepsilon}(\mathbf{u}_h), \boldsymbol{\varepsilon}(\mathbf{v}_h)) + \lambda(\boldsymbol{\nabla} \cdot \mathbf{u}_h, \boldsymbol{\nabla} \cdot \mathbf{v}_h) \\
&\quad + \alpha(\boldsymbol{\nabla} p_h, \mathbf{v}_h) + (S_\epsilon p_h, q_h) + (\alpha \boldsymbol{\nabla} \cdot \mathbf{u}_h, q_h) + \left(\frac{\kappa \tau}{\mu} \boldsymbol{\nabla} p_h, \boldsymbol{\nabla} q_h \right) ,
\end{aligned} \quad (3.7)$$

has been obtained by multiplying the second equation by the time step, τ . Integrating by parts the term $\alpha(\boldsymbol{\nabla} p_h, \mathbf{v}_h)$ and testing the resulting formulation by (\mathbf{u}_h, p_h) one obtains the following stability results.

Proposition 3.1. *It holds*

$$A((\mathbf{u}, p), (\mathbf{u}, p)) \geq \|\mathbf{u}\|_{V_h}^2 ,$$

with the norm

$$\|\mathbf{v}, q\|_{V_h}^2 = \frac{\rho}{2\tau^2} \|\mathbf{v}\|^2 + 2E\|\boldsymbol{\varepsilon}(\mathbf{v})\|^2 + S_\epsilon\|p\|^2 + \frac{\kappa\tau}{\mu} \|\boldsymbol{\nabla} p\|^2 .$$

Two remarks are important. First, it should be noted that the time derivative of the pressure and the diffusive term, $(\kappa\tau/\mu \boldsymbol{\nabla} p_h, \boldsymbol{\nabla} q_h)$, act as a stabilizer of the spatial discretization. Second, the resulting stability of $A((\mathbf{u}, p), (\mathbf{v}, q))$ strongly depends on the physical parameters, and it can indeed deteriorate – especially concerning the pressure regularity – if the mass storage coefficient S or the medium permeability κ are very small. This issue has been also investigated in [46] for the steady poroelastic case in presence of strong discontinuities in the permeability. In that setting, it has been proposed to include a stabilization term of the form $\beta(\boldsymbol{\nabla} p_h, \boldsymbol{\nabla} q_h)$, where $\beta = \beta(E, \lambda, h)$. In the physical regime relevant for this work, we did not observe stability issues related to spatial discretization. Additional numerical tests have been performed considering the stabilization proposed in [46] showing, however, only negligible differences.

Additionally, for the numerical simulations presented in this paper, we used a Newmark algorithm [47] for the discretization of the second-order time derivative in the equations, whereas a backward Euler algorithm is used for the first-order time derivatives.

4 PDE-informed MRE data assimilation

This section is devoted to the application of the data assimilation framework (outlined in Section 2 from a general perspective) to the case of brain elastography. In particular, it is presented how the displacement obtained via MRE will be assimilated into the poroelastic model detailed in Section 3 and all the practical implementation aspects of the PBDW for a joint reconstruction of displacements and

pressure fields are presented in detail. Further results concerning the validation and application of the framework are presented in Section 5.

The computation presented in these Sections have been performed using the software MAD [36, Chapter 5], which is based on the linear algebra library PETSc [48].

4.1 Data acquisition and model generation

The data assimilation pipeline employs different sources of data:

- (a) The computational model has been generated using full brain anatomical, high-resolution MPRAGE MRI data (isotropic voxel size 1 mm^3). The anatomical image data were collected from a healthy volunteer, after having their signed consent to use these for the present study. Using the raw DICOM data, the image data were segmented using open-source software 3D Slicer [49] to produce a triangulated representation of the brain and ventricles surface (exported in an STL formatted file). Subsequently, the surface mesh was loaded into Mmg [50] to generate an unstructured mesh consisting of 12,345 4-node tetrahedral finite elements.
- (b) The reconstruction is based on displacement data over a few slices of the three-dimensional brain, located as those acquired in an MRE examination. However, no assumptions on the spatial resolution of the displacement data, i.e., of the image voxels, are required.

The results shown in Section 5 are restricted to synthetic data, i.e., displacement fields generated from forward simulations on the physiological brain geometry. However, in the context of clinical routine, this type of data can be acquired via MRE. During this examination the tissue is subject to a harmonic mechanical vibration (frequency 10-50 Hz) imposed by actuators, and the tissue response is recorded via phase-contrast MRI. The internal displacement field can then be extracted from the complex phase of the acquired images.

The data assimilation algorithm, and in particular the definition of the space of measurements (Section 2.2), requires the displacement data to be registered to the anatomical brain data. Hence, the MPRAGE used for the definition of the computational mesh, and the MRE data to be assimilated, shall be acquired, on each patient, in a single examination, to minimize additional efforts for image registration. This acquisition protocol has been recently used in the framework of inversion recovery MRE (IRMRE), to estimate biophysical parameters of the gray and white matter [19]. The application of the PBDW to in vivo data, especially within IRMRE, is subject of ongoing work.

4.2 Characterization of measures

The available data is assumed to represent the three-dimensional displacement field on N_v voxels in the upper part of the brain; thus, each image contains $3 \times N_v$ measurements, i.e., one 3D vector per voxel (Figure 4).

In what follows, the imaged voxels are denoted as $\Omega_i \subset \mathbb{R}^3$ for $i = 1, \dots, N_v$. The $3 \times N_v$ linear functionals describing the observations are defined by taking the average component of the displacement vector, v , on each voxel. Namely, the basis of the space W can be then computed after solving the following set of problems: Find $w_i^j \in V_h$ such that

$$\langle w_i^j, v \rangle = \ell_i^j(v) := \int_{\Omega_i} v e_j \, dx \quad \forall v \in V_h \text{ for } i = 1, \dots, N_v \text{ and } j = 1, 2, 3, \quad (4.1)$$

where e_j the j -th component of the unit direction vector. Equations (4.1) are solved using \mathbb{P}_1 in the FEM. A modified Gram-Schmidt algorithm is used for the ortho-normalization of the reduced basis.

Remark 4.1 (Computation of W). *Space W depends on the location of the voxels, Ω_i , but not on the particular value of the measurements. Therefore, the computation of the basis for W does not depend on the particular patient, but only on the setting of the magnetic resonance image data acquisition device (i.e., the location of the acquired data). The space W can be therefore computed ‘offline,’ i.e. before the remaining steps of the data assimilation algorithm (training, model reduction, and reconstruction) are carried out.*

Remark 4.2 (Resolution of MRE data). *The procedure for constructing the measurement space W can be analogously defined for arbitrary image resolution, regardless on the size of the finite element mesh elements.*

Remark 4.3. *Notice that the form of the systems to solve depends on the underlying Hilbert structure that defines the scalar product – this is encoded in matrix M defined in equation (2.2).*

A snapshot of the considered synthetic measures is shown in Figure 4. The results shown in this work employ synthetic data, calculated computing a forward solution (Section 3.2) for a selected set of parameters and evaluating local displacement averages on a voxel of $1 \times 1 \times 1 \text{ cm}^3$ in size. This procedure leads to an image containing 600 independent observations.

Remark 4.4. *Using the formalism introduced in Section 2, for a given set of physical parameters these observations define the projection of the true state onto W , e.g.: $w = \Pi_W u_{\text{true}}$.*

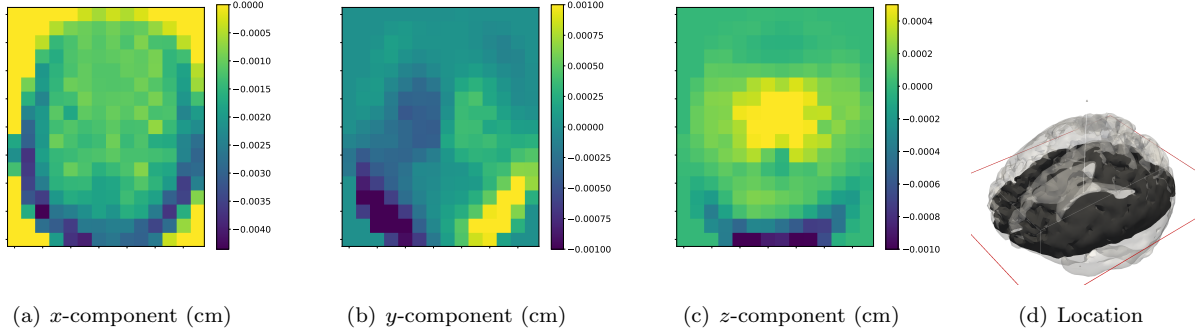


Figure 4: Figures (a), (b), and (c): Snapshot of the displacement measurements considered for the data assimilation problem (time instant: 15 ms after the pulse begins). Figure (d): Location of the measured slice with respect to the brain model.

4.3 Training set and order reduction of the model

The training manifold $\mathcal{M}^{\text{training}}$ is computed sampling uniformly the parameter space in the intervals (see also Table 1):

$$\kappa \in [10^{-9}, 10^{-8}] , E \in [10^5, 10^6] , \nu \in [0.4, 0.45] , p_{\text{ventricles}} \in [1, 1.1] \times 10^4 . \quad (4.2)$$

Note the quantities are expressed in CGS units. The parameter ranges for κ , E , and ν used in (4.2) are based on physiological parameter values obtained from relevant brain biomechanics modeling works from the literature. All remaining parameters are assumed to be given, and equal to the values specified in Table 1. For easiness of notation, in what follows the vector $\theta = (\kappa, E, \nu, p_{\text{ventricles}})$ will denote a generic element of the parameter space.

The pressure field is introduced through the forward PDE model as a boundary condition. The considered range serves to be able to capture, within the training manifold, the variability of the ventricular CSF pressure between the two selected ranges (more details will be presented in Section 5.3). The training manifold is computed numerically by solving together equations (3.6)–(3.7) using the finite element method presented in Section 3.2.

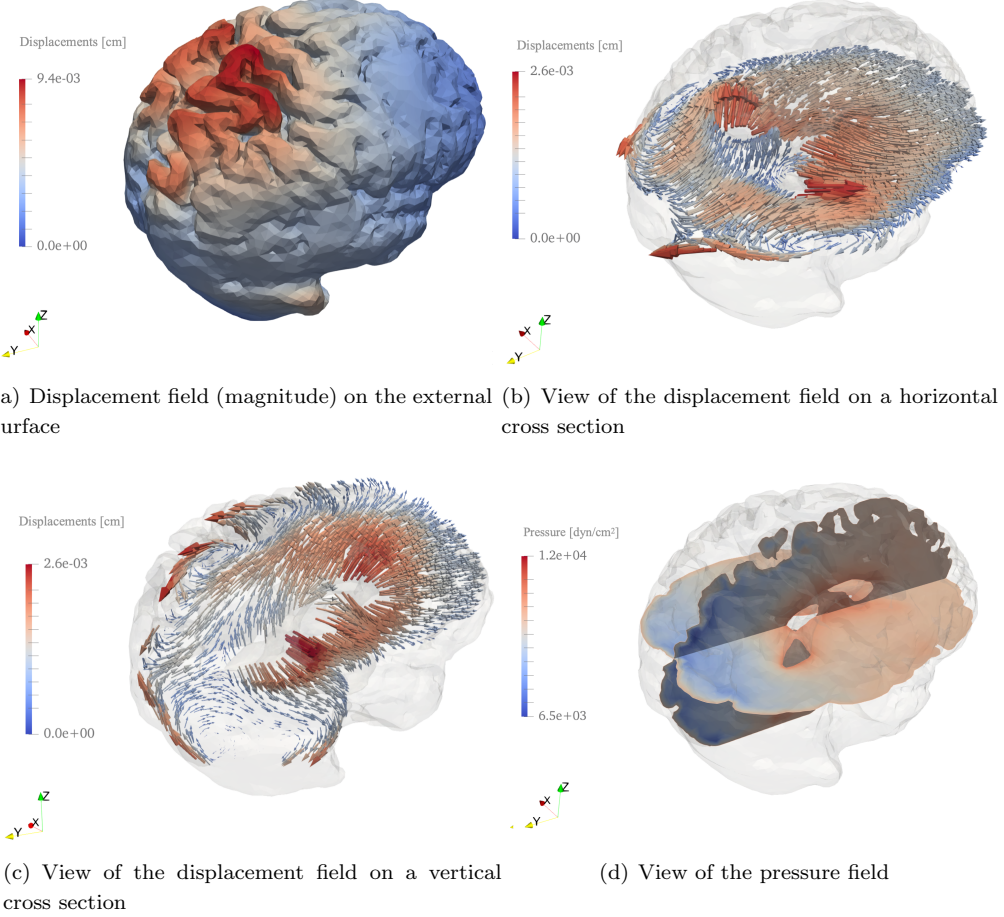
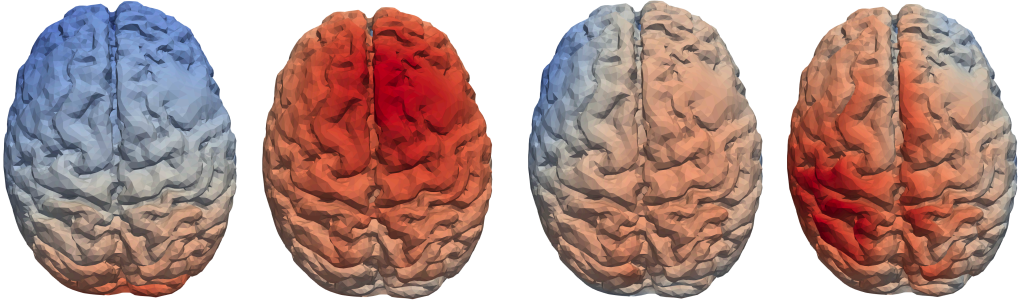


Figure 5: Snapshot of the numerical solution of (3.5) for $\nu = 0.4$, $E = 10^5$ dyn/cm² and $\kappa = 10^{-8}$ cm², 15 ms after pulse is initiated.

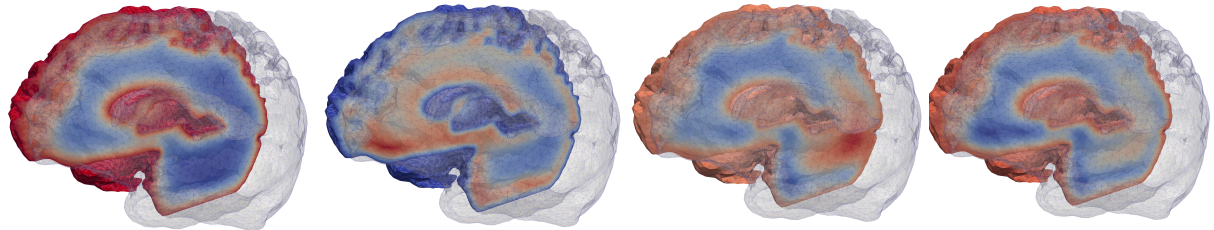
The training set manifold is defined by the outputs of 512 simulations, each one including a time series of 40 time-steps (per pulse cycle). Thus, the training manifold composes in total of $K = 20,480$ snapshots, each one being a finite element functions of dimension $\mathcal{N} \approx 131.5K$, four (degrees-of-freedom per nodal point) times the number of nodes of the FE mesh. As an example, one of the snapshots in $\mathcal{M}^{\text{training}}$ is shown in Figure 5. The computations were carried out in parallel on machines with 768 GB of RAM memory and up to 72 threads.

Subsequently, the snapshots are stored in a data matrix: $A \in \mathbb{R}^{\mathcal{N} \times K}$. The reduced basis defining the space V_n is then computed using the PCA of the snapshot matrix, as described in Section 2.4. The first four modes of both displacement and pressure fields are depicted in Figure 6

The model error (Equation (2.9); Figure 7, left) can be computed from the singular values of the



(a) View of the first four displacements modes



(b) View of the first four pressure modes

Figure 6: Basis functions (non-dimensional) of the reduced space V_n for displacement and pressure. The functions are normalized in the L^2 -norm.

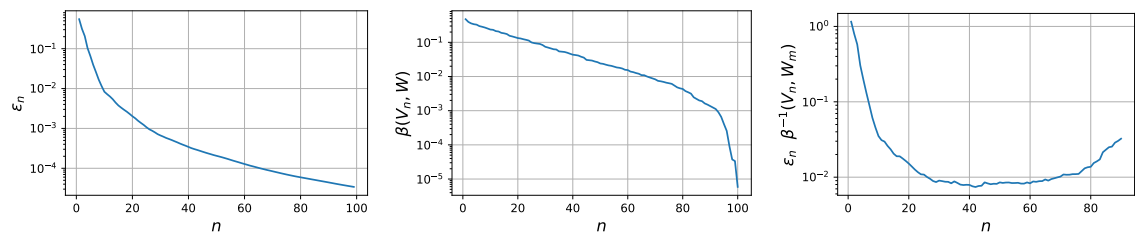


Figure 7: Left. Behavior of the PCA approximation error ϵ_n (2.9) as a function of the reduced space dimension. Center. Orientation $\beta(V_n, W)$ (2.6) (stability constant) between model and measures, as a function of the reduced space dimension n . Right. Normalized *a priori* error bound (Figure (7)) as a function of the dimension of the reduced space dimension n .

snapshot matrix. Also, constant $\beta(W, V_n)$ (2.6) (Figure 7, center) that defines the observability of the reduced model can be computed from the observation space W as a function of the dimension of the reduced-order space. The curve for the resulting error bound (2.5) as a function of the dimension of V_n is shown in Figure 7 (right). Based on this curve, the dimension of the reduced space n is then chosen as the value that minimizes the quantity $\frac{\hat{\epsilon}_n}{\beta(V_n, W)}$ ($n = 41$ in the considered case).

5 Results

5.1 Joint reconstruction of displacements and pressure

As underlined above, the purpose of the proposed data assimilation approach is the characterization of pathological pressure gradients through MRE. To facilitate inferring pressure-dependent quantities, it is necessary to apply the PBDW method for the reconstruction of both the displacement and the pressure fields.

Remark 5.1. *The main challenge of this joint reconstruction strategy is a consequence of the fact that the only the displacement data are available and the pressure state is thus completely invisible to the data assimilation algorithm. Formally, it holds $\Pi_{W_m} q = 0, \forall (v, q) \in \mathcal{M}^{\text{training}}$.*

Thus, the joint reconstruction of the MRE data is approached by considering a modified inner product on the solution space $V_h = U_h \times Q_h$:

$$\langle (u, p), (v, q) \rangle_{\zeta, V_h} := (u, v) + \zeta (p, q), \quad (5.1)$$

where constant ζ is a free parameter that is tuned to weigh equally the norms of both components. This step enhances the stability of the computation of the reduced-order model, as well as the quality of the inf-sup constant $\beta(V_n, W_m)$. In the practical computation, this parameter is defined via

$$\zeta = \frac{\max_{u \in \mathcal{M}^{\text{training}}} \|u\|_{L^2}}{\max_{p \in \mathcal{M}^{\text{training}}} \|p\|_{L^2}}.$$

The reconstruction is based on the L^2 -product, i.e., considering the ambient space V_h as a subspace of $[L^2(\Omega)]^3 \times L^2(\Omega)$. In the present work, the choice of an L^2 -product is dictated by the fact that the primary targets are the displacement and pressure fields, but not necessarily their corresponding gradient quantities. Alternatively, it is also possible to seek the reconstruction $[H^1(\Omega)]^3 \times H^1(\Omega)$, by modifying accordingly the inner product used throughout the algorithm.

5.2 Validation

The proposed MRE data assimilation algorithm is validated by reconstructing the poroelastic solution in a set of 18 physical parameters $(\kappa, E, \nu, p_{\text{ventricles}})$, not included in those used for generating the training manifold. The test parameters have been sampled from a uniformly random distribution within the range of equation (4.2), but not included in the set of the training parameters. For each test case, the displacement field on the selected plane has been observed from the forward solution to generate the synthetic measurements. Next, the overall displacement and pressure fields have been reconstructed using the reduced trained manifold space. Finally, the reconstruction errors are evaluated as defined by

$$e_{u, \theta_i} = \frac{\|u_{\theta_i, \text{true}} - u_{\theta_i}^*\|_{L^2}}{\|u_{\theta_i, \text{true}}\|_{L^2}}, \quad e_{p, \theta_i} = \frac{\|p_{\theta_i, \text{true}} - p_{\theta_i}^*\|_{L^2}}{\|p_{\theta_i, \text{true}}\|_{L^2}},$$

where $i = 1, \dots, 18$, $u_{i, \text{true}}$ and $p_{i, \text{true}}$ stand for the numerical solution of the forward problem for parameters θ_i (ground truth), and $u_{\theta_i}^*$ and $p_{\theta_i}^*$ are the corresponding PBDW reconstructions.

The joint reconstruction errors for all samples, using the metric introduced by the inner product (5.1), are shown in Figure 8. The reconstruction errors for each field considered (displacements and pressure) are shown separately in Figure 9 (left and right, respectively). In particular, it shows that the displacements are well reconstructed in all cases.

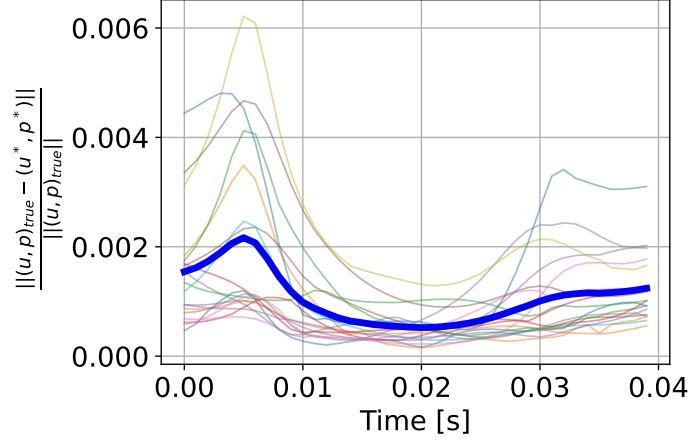


Figure 8: Joint relative L^2 reconstruction error for the 18 different test cases used for validation. The blue curve shows the average error over the 18 samples.

Moreover, we also observe that the pressure is reconstructed with satisfactory accuracy (peak errors mostly below 10% over the whole cycle), with one single case showing a peak error of the order of 15% (average error below the 5%). No correlation is observed in the quality of the approximation of the displacement when compared to that of the pressure.

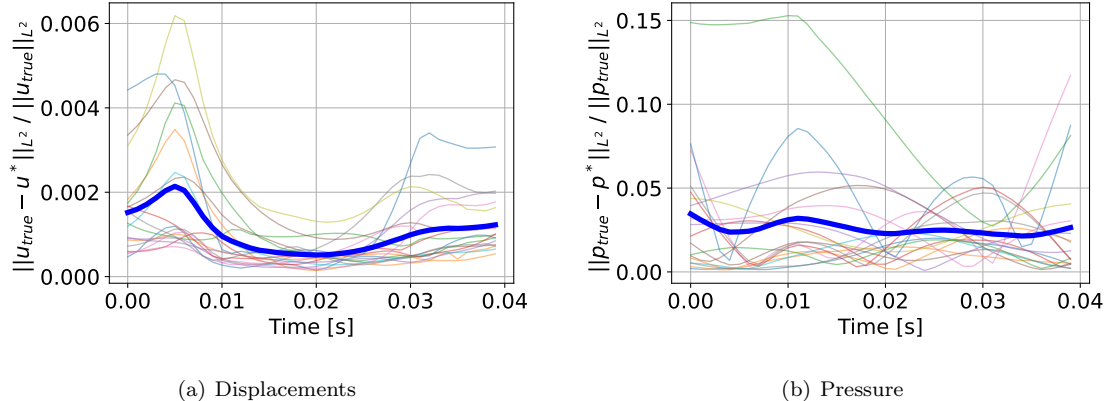


Figure 9: Relative L^2 reconstruction errors for displacement (left) and pressure (right) for the 18 samples used for validation. The blue curve shows the average error over the 18 cases.

A snapshot of the results in the scenario with the largest values for the model error (Equation (2.9)) is visualized in Figure 10 – it visually compares the reference solution, the PBDW reconstruction, and the corresponding relative difference.

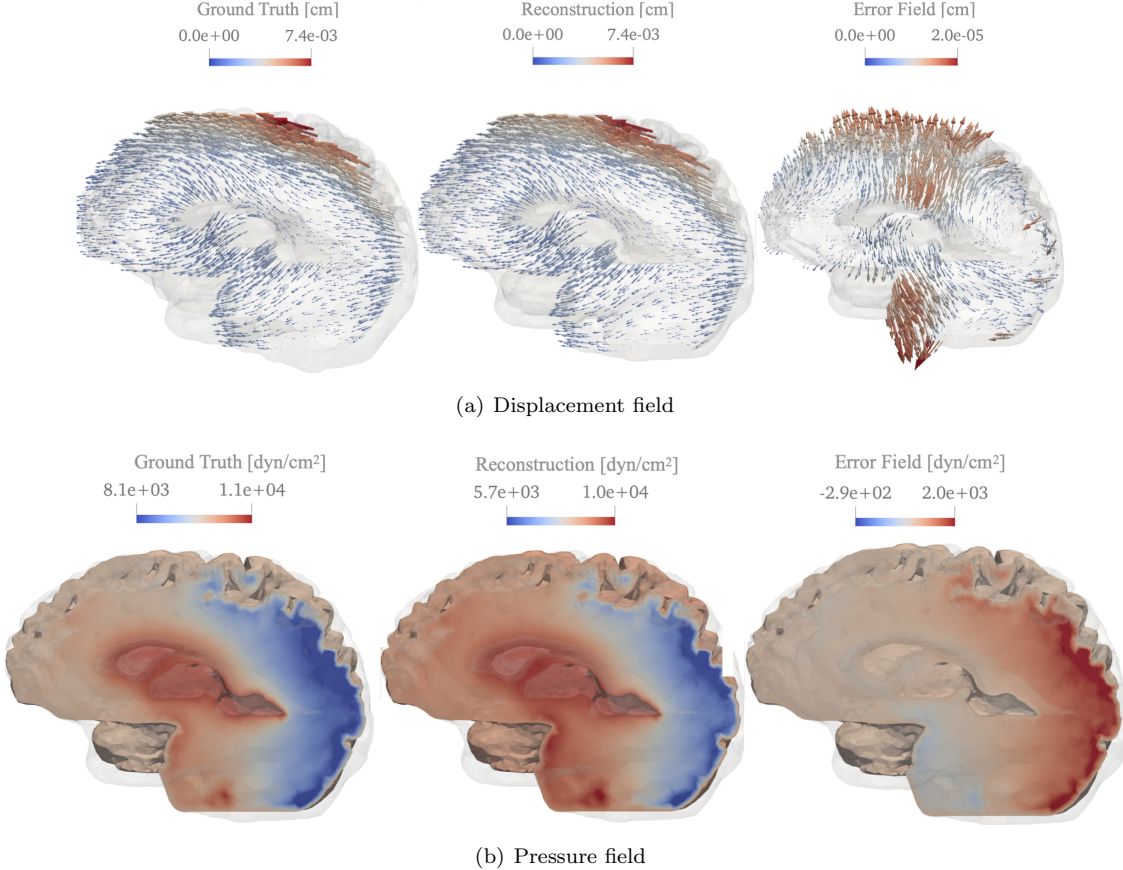


Figure 10: Reconstruction at $t = 10$ ms after the pulse start, of displacement (top) and pressure (bottom) fields for the scenario with the largest reconstruction error among the 18 samples used for the validation.

5.3 Characterization of pressure-dependent biomarkers

In this paragraph, the characterization of elevated pressure gradients from displacement data of the data assimilation algorithm is interrogated. For this purpose, the following quantity is introduced:

$$p_v(p) := \frac{1}{T} \int_0^T \left[\frac{\int_{\Gamma_{\text{ventricles}}} p(x, t) \, d\Gamma}{\int_{\Gamma_{\text{ventricles}}} d\Gamma} \right] dt, \quad (5.2)$$

which represents the average, with respect to time and over the whole surface of the ventricular CSF pressure. This indicator is important to evaluate the presence of abnormal ICP in the brain, as well as characterize increased ventricle volume.

The purpose of this numerical experiment is to test the accuracy of the ventricular pressure reconstruction (see Equation (5.2)), and interrogate the capability of the framework to stratify intracranial pressure (physiologic or pathological) by solely relying on limited displacement observations. The numerical experiment has been designed as follows. Two sets of synthetic individuals have been created, each set containing 8 individuals (16 in total). For each individual, the parameters κ , E , and ν have been sampled within the range specified in (4.2). The differentiation between physiological levels (normal) and pathological levels (increased) of ICP has been modeled by sampling the pressure boundary condition parameter within the aforementioned ranges.

$$p_{\text{ventricles}} \in [1, 1.02] \times 10^4 \text{ dyn/cm}^2, \quad (5.3)$$

for the first group (normal intracranial pressure), and

$$p_{\text{ventricles}} \in [1.08, 1.1] \times 10^4 \text{ dyn/cm}^2, \quad (5.4)$$

for the second group (increased intracranial pressure).

Hence, since the value of the outer CSF pressure is set to 10^4 dyn/cm^2 , the pathological cases (those with an increased pressure) are characterized by an ICP gradient between 800 and 1000 dyn/cm^2 (0.8 to 1 $\text{cm-H}_2\text{O}$), while the pressure difference for healthy scenarios (normal pressure) is up to 200 dyn/cm^2 (0.2 $\text{cm-H}_2\text{O}$), in line with the range of values obtained in the numerical experiments shown in [51]. For each of these 16 synthetic patients the background PDE problem (3.6)–(3.7) has been solved numerically, sampling the displacement data on a set of slices (see Figure 4). Then, the reduced-order model trained as discussed in Section 5.2 is used to reconstruct the pressure field and compute the ventricular pressure evaluating (5.2).

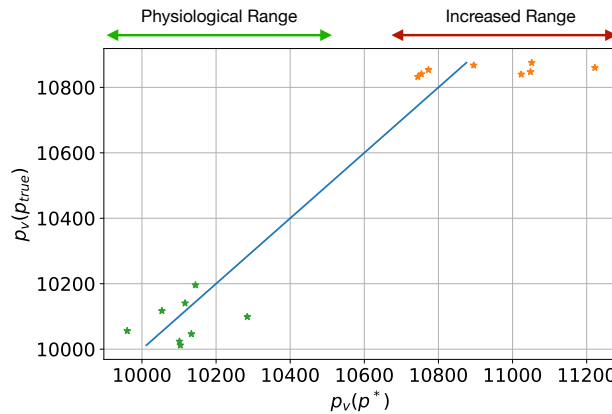


Figure 11: Reconstructed ventricular pressure (5.2) versus the values computed using the reference values for the synthetic patients. Each scenario has been labeled as "normal" or "increased", depending on the value of $p_{\text{ventricle}}$. The green dots correspond to the scenarios originally sampled from the normal range (5.3), whilst the orange dots corresponds to the simulations with elevated pressures in the range (5.4). The picture show that the algorithm is capable of separating the two regimes correctly. The blue line corresponds to the line $p^* = p_{\text{true}}$, and the distance on the x -axis between each point and the blue line shows the absolute reconstruction error. In particular, the largest error obtained among the normal-pressure scenario is of 300 dyn/cm^2 (less 2% of of the ventricular pressure in that particular case), while the largest error among the simulations with increased pressures is of 370 dyn/cm^2 (about 3%).

The results for the ventricular pressure reconstruction simulations are shown in Figure 11. As such, ventricular pressure can be evidently classified between normal and increased levels of pressure based on the reconstructed values. Furthermore, the illustration confirms the accuracy of the reconstruction algorithm by comparing the estimated ventricular pressure with the one computed from the true ventricular pressure solution, p_{true} . The relative errors reported here are below 2% for the scenarios with normal pressure levels, and about 3% for the scenarios with increased pressure levels.

6 Conclusions

This contribution presents a novel *in silico* procedure of the Parametrized-Background Data-Weak (PBDW) method for the assimilation of medical imaging data. In this contribution, we focused assimilating pertinent displacement data produced through magnetic resonance elastography of the human brain. The main contribution of the proposed approach is the possibility of characterizing non-invasively intracranial pressure from partially available displacement data. PBDW data assimilation is used to reconstruct, from the available observations, displacement and pressure fields in the whole domain. The procedure is based on anatomical images – used to generate a personalised computational model of the brain organ – a finite element method for solving the underlying tissue poroelastic mechanics, and a range for the values of the mechanical parameters. From the reconstructed pressure field, it is then possible to extract clinically relevant biomarkers. The method naturally handles partially available data and uncertainty in the physical parameters, and it can therefore overcome challenges due to missing information (e.g., pressure boundary conditions), and cope with image acquisition constraints (e.g., location of data, typically limited to one or few slices in the case of elastography). Moreover, since the physical solution is reconstructed in the whole domain, the proposed approach can estimate quantity of interests also when the region of interest is not observed directly.

The accuracy of the data assimilation for the joint state reconstruction (for both displacement and pressure) has been investigated in detail. The algorithm has been validated considering 18 cases sampled within a parameter space including mechanical parameters (Young modulus, Poisson modulus, tissue permeability), and CSF pressure. The simulation experiments demonstrated that including the CSF ventricular pressure in the training step, in which the manifold and the corresponding reduced space are computed, is capable to identify patients with increased ventricular pressure based solely on partially available displacement data.

With the purpose of validating the data assimilation framework, this work considers synthetic displacement data. However, the elastography data acquisition is part of a recent protocol used in medical imaging research in combination of inversion recovery (IR) protocols for the identification of tissue porosity maps [19, 38]. The validation for the available *in vivo* data is planned for a follow-up work. However, further improvements of the proposed data assimilation algorithm that will be addressed in future research efforts include the use of a nonlinear tissue biomechanics (e.g., viscoelasticity), anisotropic constitutive models, or by enhancing the modeling through multiscale formulations (e.g., [52, 53]). Also, other challenging extensions of the presented research concerns the possibility of tackle the reconstruction of the ICP gradient, instead of the whole pressure field. Including measurements from tomo-elastography [54] or ultrasound elastography [14] into the training phase will considerably improve the proposed data assimilation approach and help towards clinical translation.

Acknowledgments

This research is funded by the Deutsche Forschungsgemeinschaft (DFG, German Research Foundation) under Germany’s Excellence Strategy - MATH+: The Berlin Mathematics Research Center [EXC-2046/1 - project ID: 390685689]. V.V. wishes to acknowledge the financial support of the Cyprus Cancer Research Institute through the Bridges in research excellence CCRI_2020_FUN_001, Project “PROTEAS” [grant ID: CCRI_2021_FA.LE.105].

References

- [1] R. Muthupillai, D.J. Lomas, P.J. Rossman, J.F. Greenleaf, A. Manduca, and R.L. Ehman. Magnetic resonance elastography by direct visualization of propagating acoustic strain waves. *Science*, 269:1854–1857, 1995.
- [2] D. Fovargue, D. Nordsletten, and R. Sinkus. Stiffness reconstruction methods for MR elastography. *NMR in Biomedicine*, 2018.
- [3] I. Sack, B. Beierbach, U. Hamhaber, D. Klatt, and J. Braun. Non-invasive measurement of brain viscoelasticity using magnetic resonance elastography. *NMR Biomed.*, 21(3):265–271, 2008.
- [4] I. Sack and T. Schäffter, editors. *Quantification of Biophysical Parameters in Medical Imaging*. Springer, 2018.
- [5] A. Manduca, P.J. Bayly, E.L. Ehman, A. Kolipaka, T.J. Royston, I. Sack, R. Sinkus, and B.E. Van Beers. MR elastography: Principles, guidelines, and terminology. *Magnetic Resonance in Medicine*, 85:2377–2390, 2021.
- [6] G. Bertalan, C. Klein, S. Schreyer, B. Steiner, B. Kreft, H. Tzschätzsch, A. Ariza, M. Nieminen-Kelhä, J. Braun, J. Guo, and I. Sack. Biomechanical properties of the hypoxic and dying brain quantified by magnetic resonance elastography. *Acta Biomaterialia*, 101:395 – 402, 2020.
- [7] R. Reiter, M. Shahryari, H. Tzschätzsch, D. Klatt, B. Siegmund, B. Hamm, and P. Asbach. Spatial heterogeneity of hepatic fibrosis in primary sclerosing cholangitis vs. viral hepatitis assessed by MR elastography. *Scientific Reports*, 11(1):1–8, 2021.
- [8] K. J. Streitberger, L. Lilaj, F. Schrank, J. Braun, K. T. Hoffmann, M. Reiss-Zimmermann, and I. Sack. How tissue fluidity influences brain tumor progression. *Proceedings of the National Academy of Sciences*, 117(1):128–134, 2020.
- [9] A. Bunevicius, K. Schregel, R. Sinkus, A. Golby, and S. Patz. Review: Mr elastography of brain tumors. *Neuroimage Clin.*, 25:102109, 2020.
- [10] L.V. Hiscox, C.L. Johnson, E. Barnhill, M.D. McGarry, J. Huston, E.J. van Beek, J.M. Starr, and N. Roberts. Magnetic resonance elastography (MRE) of the human brain: technique, findings and clinical applications. *Phys Med Bio.*, 61:R401–R437, 2016.
- [11] J. Ren, X. Wu, J. Huang, X. Cao, Q. Yuan, Zhang. D., Z. Du, P. Zhong, and J. Hu. Intracranial Pressure Monitoring-Aided Management Associated with Favorable Outcomes in Patients with Hypertension-Related Spontaneous Intracerebral Hemorrhage. *Transl Stroke Res.*, 11(6):1253–1263, 2020.
- [12] N. Fattahi, A. Arani, . Perry, A, F. Meyer, A. Manduca, K. Glaser, M.L. Senjem, R.L. Ehman, and J. Huston. MR elastography demonstrates increased brain stiffness in normal pressure hydrocephalus. *American Journal of Neuroradiology*, 37(3):462–467, 2016.
- [13] J.S. Aunan-Diop, C.B. Pedersen, B. Halle, U. Jensen, S. Munthe, F. Harbo, B. Johannsson, and F.R. Poulsen. Magnetic resonance elastography in normal pressure hydrocephalus—a scoping review. *Neurosurg Rev*, 45:1157–1169, 2022.
- [14] B. Kreft, H. Tzschätzsch, M. Sharyari, P. Haffner, J. Braun, I. Sack, and K.-J. Streitberger. Non-invasive Detection of Intracranial Hypertension by Novel Ultrasound Time-Harmonic Elastography. *Investigative Radiology*, 57:77–84, 2022.
- [15] S. Hirsch, J. Guo, R. Reiter, E. Schott, C. Büning, R. Somasundaram, J. Braun, I. Sack, and T.J. Kroencke. Towards compression-sensitive magnetic resonance elastography of the liver: sensitivity of harmonic volumetric strain to portal hypertension. *J. Magn. Reson. Imaging*, 39(2):298–306, 2014.

- [16] S. Hetzer, P. Birr, A. Fehlner, S. Hirsch, F. Dittmann, E. Barnhill, J. Braun, and I. Sack. Perfusion alters stiffness of deep gray matter. *J Cereb Blood Flow Metab.*, 38(1):116–125, 2018.
- [17] L.M. Solamen, M.D.J. McGarry, J. Fried, J.B. Weaver, S.S. Lolis, and K.D. Paulsen. Poroelastic mechanical properties of the brain tissue of normal pressure hydrocephalus patients during lumbar drain treatment using intrinsic actuation mr elastography. *Academic Radiology*, 28(4):457–466, 2021.
- [18] M.D. McGarry, E.E. Van Houten, L. Solamen, S. Gordon-Wylie, J.B. Weaver, and K.D. Paulsen. Uniqueness of poroelastic and viscoelastic nonlinear inversion MR elastography at low frequencies. *Phys. Med. Biol.*, 64:075006, 2019.
- [19] L. Lilaj, T. Fischer, J. Guo, J. Braun, I. Sack, and S. Hirsch. Separation of fluid and solid shear wave fields and quantification of coupling density by magnetic resonance poroelastography. *Mag. Res. Med.*, 85(3):1655–1668, 2021.
- [20] R. Leiderman, P.E. Barbone, A.A. Oberai, and J.C. Bamber. Coupling between elastic strain and interstitial fluid flow: ramifications for poroelastic imaging. *Phys. Med. Biol.*, 51:6291–6313, 2006.
- [21] M.D. McGarry, C.L. Johnson, B.P. Sutton, J.G. Georgiadis, E.E. Van Houten, A.J. Pattison, J.B. Weaver, and K.D. Paulsen. Suitability of poroelastic and viscoelastic mechanical models for high and low frequency mr elastography. *Med. Phys.*, 42(2):947–957, 2015.
- [22] A.J. Pattison, M.D. McGarry, J.B. Weaver, and K.D Paulsen. Spatially-resolved hydraulic conductivity estimation via poroelastic magnetic resonance elastography. *IEEE Trans. Med. Imag.*, 33:1373–1380, 2014.
- [23] S. Budday, G. Sommer, C. Birk, C. Langkammer, J. Haybaeck, J. Kohnert, M. Bauer, F. Paulsen, P. Steinmann, E. Kuhl, and G.A. Holzapfel. Mechanical characterization of human brain tissue. *Acta Biomaterialia*, 48:319–340, 2017.
- [24] R. de Rooij and E. Kuhl. Constitutive modeling of brain tissue: current perspectives. *Appl. Mech. Rev.*, 68:010801, 2016.
- [25] T. Dutta-Roy, A. Wittek, and K. Miller. Biomechanical modelling of normal pressure hydrocephalus. *Journal of Biomechanics*, 41(10):2263–2271, 2008.
- [26] E. Comellas, J.-P. Budday, S. Pelteret, G.A. Holzapfel, and P. Steinmann. Modeling the porous and viscous responses of human brain tissue behavior. *Computer Methods in Applied Mechanics and Engineering*, 369:113128, 2020.
- [27] S. Budday, T. C. Ovaert, G. A. Holzapfel, P. Steinmann, and Kuhl E. Fifty shades of brain: A review on the mechanical testing and modeling of brain tissue. *Archives of Computational Methods in Engineering*, 27:1187–1230, 2020.
- [28] S. Hirsch, J. Braun, and I. Sack. *Magnetic Resonance Elastography: Physical Background And Medical Applications*. Wiley, 2017.
- [29] P.R. Perriñez, F.E. Kennedy, E.E.W. Van Houten, J.B. Weaver, and K.D. Paulsen. Modeling of soft Poroelastic tissue in time-harmonic MR Elastography. *IEEE Trans Biomed Eng*, 56(3):598–608, 2009.
- [30] P.R. Perrinez, A.J. Pattison, F.E. Kennedy, J.B. Weaver, and K.D. Paulsen. Contrast detection in fluid-saturated media with magnetic resonance poroelastography. *Med. Phys.*, 37:3518–3526, 2010.
- [31] L. Tan, M. D. J. McGarry, E. W. Van Houten, M. Ji, L. Solamen, W. Zeng, J.B. Weaver, and K. D. Paulsen. A numerical framework for interstitial fluid pressure imaging in poroelastic MRE. *PLOS ONE*, 12(6):1–22, 06 2017.

[32] D. Fovargue, S. Kozerke, R. Sinkus, and D. Nordsletten. Robust MR elastography stiffness quantification using a localized divergence free finite element reconstruction. *Medical Image Analysis*, 44:126–142, 2018.

[33] D. Fovargue, Fiorito M., A. Capilasio, D. Nordsletten, J. Lee, and R. Sinkus. Towards noninvasive estimation of tumour pressure by utilising MR elastography and nonlinear biomechanical models: a simulation and phantom study. *Scientific Report*, 10:5588, 2020.

[34] Y. Maday, A.T. Patera, J.D. Penn, and M. Yano. A Parameterized-Background Data-Weak approach to variational data assimilation: formulation, analysis, and application to acoustics. *Int. J. Num. Methods Engr.*, 102(5):933–965, 2014.

[35] F. Galarce, J.F. Gerbeau, D. Lombardi, and O. Mula. Fast reconstruction of 3D blood flows from Doppler ultrasound images and reduced models. *Computer Methods in Applied Mechanics and Engineering*, 375:113559, 2021.

[36] F. Galarce Marin. *Inverse problems in hemodynamics. Fast estimation of blood flows from medical data.* <https://gitlab.com/felipe.galarce.m/mad/>. PhD thesis, INRIA Paris & Laboratoire Jacques-Louis Lions. Sorbonne Université, 2021.

[37] F. Galarce, D. Lombardi, and O. Mula. State estimation with model reduction and shape variability. application to biomedical problems. *SIAM Journal on Scientific Computing*, 2022.

[38] L. Lilaj, H. Herthum, T. Meyer, M. Shahryari, G. Bertalan, A. Caiazzo, J. Braun, T. Fischer, S. Hirsch, and I. Sack. Inversion recovery MR elastography of the human brain for improved stiffness quantification near fluid-solid boundaries. *Mag. Res. Med.*, 86(5):2552–2561, 2021.

[39] Y. Maday, A. T. Patera, J. D. Penn, and M. Yano. A parameterized-background data-weak approach to variational data assimilation: formulation, analysis, and application to acoustics. *International Journal for Numerical Methods in Engineering*, 102(5):933–965, 2015.

[40] F. Galarce, D. Lombardi, and O. Mula. Reconstructing haemodynamics quantities of interest from Doppler ultrasound imaging. *Int. J. Numer. Meth. Biomedical Eng.*, 2021.

[41] P. Binev, A. Cohen, W. Dahmen, R. DeVore, G. Petrova, and P. Wojtaszczyk. Data assimilation in reduced modeling. *SIAM/ASA Journal on Uncertainty Quantification*, 5(1):1–29, 2017.

[42] M. Rathinam and L.R. Petzold. A new look at proper orthogonal decomposition. *SIAM Journal on Numerical Analysis*, 41(5):1893–1925, 2003.

[43] I. Smillie, I. Sobey, and Molnar Z. A hydroelastic model of hydrocephalus. *Journal of Fluid Mechanics*, 539, 2005.

[44] S. Hirsch, J. Braun, and I. Sack. *Magnetic Resonance Elastography: Physical Background and Medical Applications*. Wiley, 2017.

[45] T. Bogoslovsky, J. Gill, A. Jeromin, C. Davis, and R Diaz-Arrastia. Fluid biomarkers of traumatic brain injury and intended context of use. *Diagnostics (Basel, Switzerland)*, 6, 2016.

[46] C. Rodrigo, F.J. Gaspar, X. Hu, and L.T. Zikatanov. Stability and monotonicity for some discretizations of the Biot’s consolidation model. *Computer Methods in Applied Mechanics and Engineering*, 298:183–204, 2016.

[47] N. Newmark. A method of computation for structural dynamics. *Journal of the Engineering Mechanics Division*, 85:67–94, 1959.

[48] S. Balay, S. Abhyankar, Adams. M.D., J. Brown, P. Brune, K. Buschelman, L. Dalcin, V. Eijkhout, W.D. Gropp, D. Kaushik, M.G. Knepley, L.C. McInnes, K. Rupp, B.F. Smith, S. Zampini, and H. Zhang. PETSc Web page. <http://www.mcs.anl.gov/petsc>, 2015.

- [49] A. Fedorov, R. Beichel, J. Kalpathy-Cramer, J. Finet, J-C. Fillion-Robin, S. Pujol, C. Bauer, D. Jennings, F.M. Fennessy, M. Sonka, J. Buatti, S.R. Aylward, J.V. Miller, S. Pieper, and R Kikinis. 3D slicer as an image computing platform for the quantitative imaging network. *Magnetic Resonance Imaging.*, 30, 2012.
- [50] C. Dapogny, C. Dobrzynski, and P. Frey. Three-dimensional adaptive domain remeshing, implicit domain meshing, and applications to free and moving boundary problems. *J. Comp. Phys.*, 262:358–378, 2014.
- [51] X. Li, H. von Holst, and S. Kleiven. Influences of brain tissue poroelastic constants on intracranial pressure (ICP) during constant-rate infusion. *Comp. Meth. Biomech. Biomed. Engnr.*, 16(12):1330–1343, 2014.
- [52] L. Heltai and A. Caiazzo. Multiscale modeling of vascularized tissues via nonmatching immersed methods. *Int. J. Numer. Methods Biomed. Engnr.*, 35(12), 2019.
- [53] L. Heltai, A. Caiazzo, and L.O. Müller. Multiscale coupling of one-dimensional vascular models and elastic tissues. *Ann Biomed Eng.*, 49(12):3243–3254, 2021.
- [54] M. Shahryari, Tzschätzsch. H., J. Guo, S.R. Marticorena Garcia, G. Böning, U. Fehrenbach, L. Stencel, P. Asbach, B. Hamm, J.A. Käs, J. Braun, T. Denecke, and I. Sack. Tomoelastography distinguishes noninvasively between benign and malignant liver lesions. *Cancer Res.*, 79(22):5704–5710, 2019.